

A wireless body area sensor network based on stretchable passive tags

Simiao Niu ^{1,8}, Naoji Matsuhisa^{1,2,8}, Levent Beker¹, Jinxing Li¹, Sihong Wang^{1,7}, Jiechen Wang³, Yuanwen Jiang ¹, Xuzhou Yan ¹, Youngjun Yun^{1,4}, William Burnett⁵, Ada S. Y. Poon⁶, Jeffery B.-H. Tok ¹, Xiaodong Chen ^{2*} and Zhenan Bao ^{1*}

A body area sensor network (bodyNET) is a collection of networked sensors that can be used to monitor human physiological signals. For its application in next-generation personalized healthcare systems, seamless hybridization of stretchable on-skin sensors and rigid silicon readout circuits is required. Here, we report a bodyNET composed of chip-free and battery-free stretchable on-skin sensor tags that are wirelessly linked to flexible readout circuits attached to textiles. Our design offers a conformal skin-mimicking interface by removing all direct contacts between rigid components and the human body. Therefore, this design addresses the mechanical incompatibility issue between soft on-skin devices and rigid high-performance silicon electronics. Additionally, we introduce an unconventional radiofrequency identification technology where wireless sensors are deliberately detuned to increase the tolerance of strain-induced changes in electronic properties. Finally, we show that our soft bodyNET system can be used to simultaneously and continuously analyse a person's pulse, breath and body movement.

A body area sensor network (bodyNET) enables wireless transmission of multiple human physiological signals to the digital world in a continuous and accurate fashion^{1–3}. The bodyNET system is a network of on-body sensors and external circuits for signal readout, conditioning and wireless transmission. To realize the full potential of the system, seamless hybridization between sensors and readout electronics is required. BodyNETs based on rigid sensors have already been demonstrated, thanks to fabrication compatibility with existing integrated circuit technologies^{4,5}. However, the integration of soft on-skin sensors into the bodyNET remains a key challenge. The development of such a soft bodyNET would allow the signal integrity of physiological activities and wear comfort to be significantly improved, with good skin conformability of lightweight, soft and stretchable materials^{6–24}. So far, the integration of rigid silicon circuits and stretchable sensors on a single substrate has only been achieved through the introduction of rigid islands and stretchable interconnects^{25–33}. However, the weak interfaces between soft and rigid parts severely compromised the robustness of the systems. In particular, the modulus mismatch induced concentrated strains at the interfaces, which ultimately led to delamination and mechanical failure. Therefore, physical separation of stretchable sensors from rigid readout circuits, and the elimination of all fragile interfaces, could be an effective strategy towards an intimate and robust bodyNET system.

In this Article, we report a bodyNET system composed of stretchable sensors attached on multiple skin locations to gather human physiological and movement signals, which are wirelessly operated by silicon readout circuits attached to textiles. The physically separated stretchable sensors and silicon readout circuit communicate via passive radiofrequency identification (RFID) technology.

The stretchable sensor tags are fabricated by printing intrinsically stretchable materials on elastic substrates, and are completely free from rigid silicon chips and batteries to avoid potential stress-concentrated regions and improve system robustness. The main technical challenge encountered here is dealing with the strain-induced changes of the sensor antenna inductance and resistance, which can affect readout effectiveness. We address this by adapting an unconventional detuned RFID tag design and verify its appropriateness through simulation and experiments. Our design enables the bodyNET system to maintain full functionality even when the on-skin sensors are stretched to 50% strain. Our bodyNET system is demonstrated by connecting multiple sensor nodes and a smartphone through Bluetooth. Our hands-free bodyNET could continuously, simultaneously and accurately monitor a person's respiration, pulse and body movements. The platform offers a powerful tool for analysing relevant human activities and physiological signals, and could potentially be used for real-time physiological studies.

Simulation and design of the system architecture

The design of our wearable bodyNET system, consisting of multiple sensor nodes positioned in various body locations to collect human physiological signals, is shown in Fig. 1. Each sensing node contains two physically separated parts that are wirelessly coupled using RFID: a stretchable on-skin sensor (target) and flexible on-textile readout circuitry (initiator) (Fig. 1a). The soft target is made of a stretchable inductor, a stretchable capacitor and a resistive strain sensor. Unlike stretchable sensor systems that use Bluetooth (Fig. 1b), there are no rigid components (for example, chips and batteries) inside the on-skin soft sensor tags, which improves the robustness and conformability of the design. Moreover, compared

¹Department of Chemical Engineering, Stanford University, Stanford, CA, USA. ²Innovative Center for Flexible Devices (iFLEX), School of Materials Science and Engineering, Nanyang Technological University, Singapore, Singapore. ³Department of Materials Science and Engineering, Stanford University, Stanford, CA, USA. ⁴Samsung Advanced Institute of Technology, Yeongtong-gu, Suwon-si, Gyeonggi-do, Republic of Korea. ⁵Department of Mechanical Engineering, Stanford University, Stanford, CA, USA. ⁶Department of Electrical Engineering, Stanford University, Stanford, CA, USA. ⁷Present address: Pritzker School of Molecular Engineering, the University of Chicago, Chicago, IL, USA. ⁸These authors contributed equally: Simiao Niu, Naoji Matsuhisa. *e-mail: chenxd@ntu.edu.sg; zbao@stanford.edu

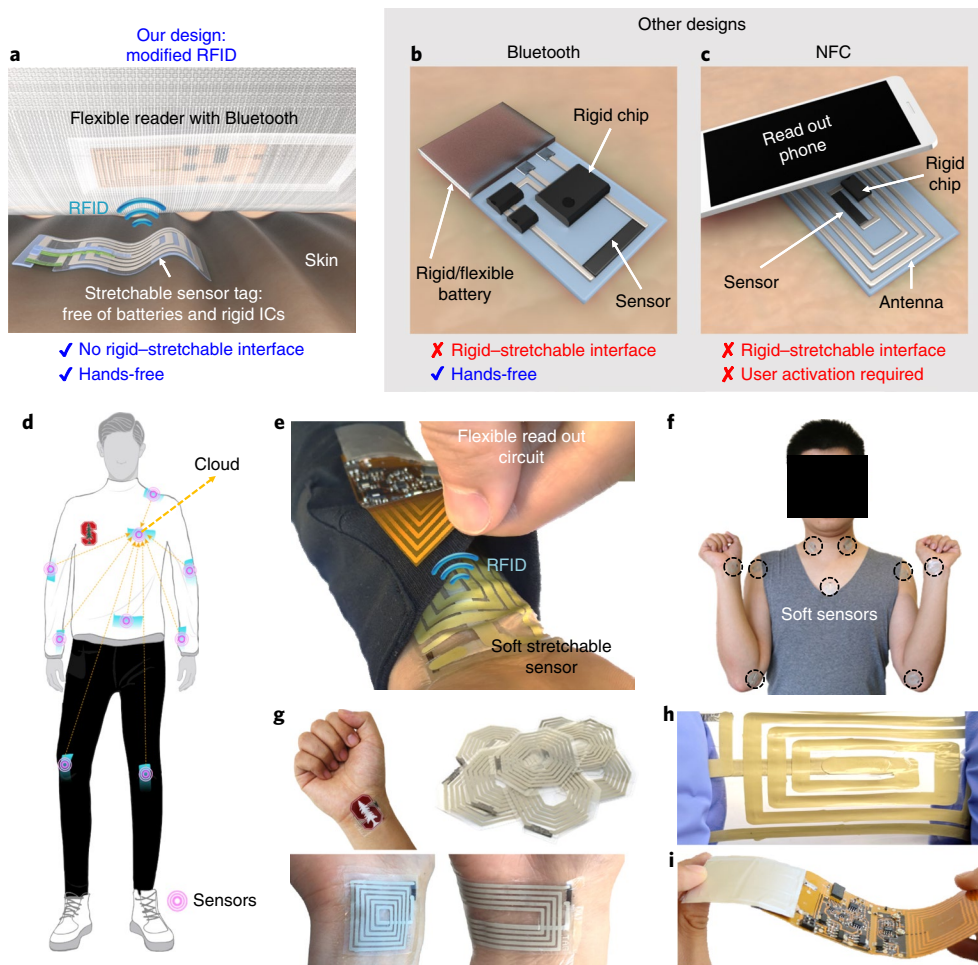


Fig. 1 | A bodyNET consisting of stretchable on-skin sensors and flexible silicon circuits on clothes. **a**, Schematic to describe a sensor node in our design that thoroughly eliminates the interconnect between rigid and soft components. A stretchable sensor is conformably attached on skin and collects the signals. The information is wirelessly read out by a flexible printed circuit board (FPCB) initiator on clothing. **b, c**, Schematics for conventional Bluetooth (**b**) and NFC (**c**) designs that have been developed previously for wearable sensors. **d**, Design concept of the bodyNET. **e**, Photograph of one sensor node for sensing the pulse on a human wrist. **f**, Photograph of a person wearing multiple skin sensors. **g**, Photograph of on-skin sensors with different designs. **h**, Photograph of a stretched target. **i**, Photograph of a bent FPCB initiator.

with a battery-free near-field communication (NFC) system (Fig. 1c)^{32,34}, both our targets and initiators (Fig. 1d,e) are fully wearable and mobile and can provide continuous and hands-free monitoring of physiological signals. The soft targets can be shaped into different sizes and placed at different body locations depending on the application (Fig. 1f–h). The initiator is composed of an antenna, signal readout circuits and flexible batteries (Fig. 1i). Desired information, such as respiration, heartbeat and motion, is first captured by the strain sensor in the on-skin wireless tag and is subsequently transmitted to the on-textile initiator by RFID transmission at a fixed operation frequency (f_{op}) of 13.56 MHz. Although the approach of sweeping f_{op} to read out resonance changes in target antennas using a vector network analyser (VNA) has been reported⁸, this approach is not suitable for wearables, as VNAs are too bulky. Additionally, the frequency band resources are limited and sweeping f_{op} over a broad range is legally prohibited.

The major design challenge for on-skin RFIDs is the strain-induced changes in the electronic properties of the stretchable targets, which could then influence the RFID readout. Accordingly, we first performed simulations to elucidate an ‘optimized’ system design (Fig. 2a; for details see Methods). Three parameters are important in this simulation: the target resonant frequency (f_{tag}), the target antenna quality factor (Q) and the coupling factor between

the initiator and target inductors (κ). f_{tag} and Q are dependent on the target inductance (L_{tag}), capacitance (C_{tag}) and internal resistance (R_{tag}) (equation (1)); external strain deformations will change these values^{8,35}) and κ is mainly dependent on the separation distance between the two inductors, where a close separation provides a large κ :

$$Q = \frac{2\pi f_{op} L_{tag}}{R_{tag}} \quad f_{tag} = \frac{1}{2\pi \sqrt{L_{tag} C_{tag}}} \quad (1)$$

Our simulation goal is to maximize the response of the voltage signal amplitude in the initiator inductor ($|V_{initiator}|$) when the sensor resistance (R_{sensor}) changes, which is illustrated as the slope of the $|V_{initiator}|$ – R_{sensor} curve (defined as gain G). Figure 2b shows that the gain is large only when $R_{sensor} < 1,000 \Omega$ and f_{tag} is exactly 13.56 MHz or > 25 MHz. The gain at $R_{sensor} = 700 \Omega$ is further investigated under different values of κ and f_{tag} in Fig. 2c, which clearly shows that there are two high gain regimes ($|G| > 1 \text{ mV } \Omega^{-1}$) in which we can operate the wireless sensors. Regime I, which is widely used in conventional resonant RFID targets, is located at relatively low κ (~ 0.1) and f_{tag} of exactly 13.56 MHz. Regime II is located at relatively high κ (> 0.2) and f_{tag} higher than 30 MHz (detuned RFID target). Regime II has a much broader frequency window ($|G| > 1 \text{ mV } \Omega^{-1}$

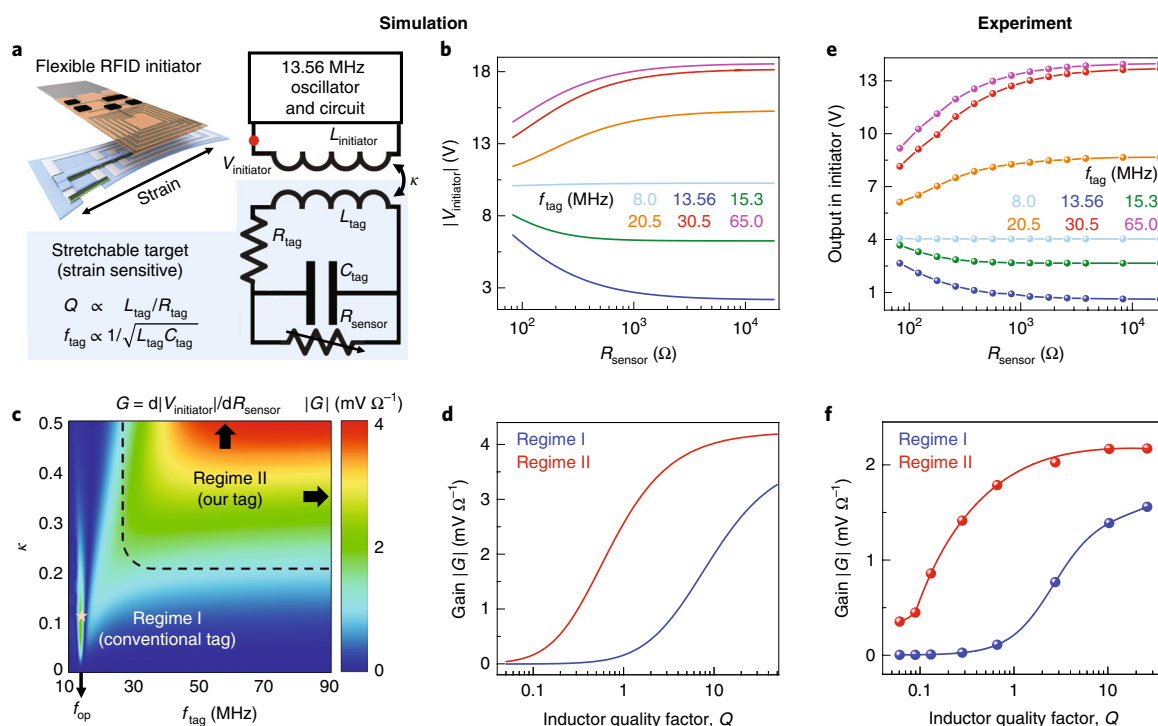


Fig. 2 | Design and experimental verification for the stretchable RFID system. **a–d.** Simulations for the radiofrequency identification (RFID) system. **a.** Simplified circuit diagram. **b.** Amplitude of the wirelessly received signal on the initiator side ($|V_{\text{initiator}}|$) for targets with different f_{tag} and R_{sensor} ($\kappa = 0.2$ and $Q = 10$). **c.** Influence of f_{tag} and κ on G . G is calculated from the slope of the $|V_{\text{initiator}}| - R_{\text{sensor}}$ curves at $R_{\text{sensor}} = 700 \Omega$. There are two distinct operation regimes to obtain high G (regimes I and II). **d.** Comparison of the tolerance of Q drop for two typical cases in each operation regime. Regime I is simulated at $f_{\text{tag}} = 13.56$ MHz and $\kappa = 0.1$. Regime II is simulated at $f_{\text{tag}} = 65$ MHz and $\kappa = 0.5$. **e, f.** Experimental measurement results to verify the simulation of **b** and **d**, respectively. In **e**, the separation distance between the target and initiator is 12 mm. The measured output voltage is the demodulated signal after the envelope detector from the flexible initiator side. In **f**, the data for regime I is measured at $f_{\text{tag}} = 13.56$ MHz and the separation distance between the target and initiator is 21 mm. The data for regime II is measured at $f_{\text{tag}} = 65.0$ MHz and the corresponding separation distance is 6 mm.

when $f_{\text{tag}} > 26.17$ MHz), so it is more tolerant against a change in f_{tag} than the conventionally used regime I ($|G| > 1 \text{ mV } \Omega^{-1}$ only when $12.75 \text{ MHz} < f_{\text{tag}} < 14.32 \text{ MHz}$). Additionally, operation in regime II offers better tolerance of Q than in regime I (Fig. 2d). When Q drops to 0.5, regime II shows a high gain of $2.18 \text{ mV } \Omega^{-1}$ while regime I only shows $0.17 \text{ mV } \Omega^{-1}$.

The high gain and tolerance of f_{tag} and Q make regime II much more favourable for our applications, as both the target and initiator can be tightly coupled (large κ) due to the close proximity between the stretchable sensors and readout circuits (that is, skin to clothes). Additionally, the large κ requirement in regime II allows a single target to be selectively read out by a close initiator, thus avoiding interference from neighbouring sensing nodes. In contrast, although regime I can maximize the gain and wireless power transmission capability under weak coupling conditions, the performance in regime I in our large κ scenarios is limited by the strong target-initiator loading effect³⁶. The above simulation was also verified by corresponding experiments (Fig. 2e, f; for details see Methods).

The specification of each target component (L_{tag} , C_{tag} , R_{tag} and R_{sensor}) in our bodyNET was determined by the above simulations. First, L_{tag} needs to be large enough ($> 100 \text{ nH}$) to provide high gain (Supplementary Fig. 3i). C_{tag} can then be small (several pF) and variable to generate $f_{\text{tag}} > 30$ MHz. This less stringent requirement for C_{tag} allows the capacitor dielectrics to be thicker ($\sim 100 \mu\text{m}$) with tolerance of even 100% variations, thus reducing fabrication difficulties and improving target reliability under strain. In contrast, an exact dielectric thickness of $\sim 2 \mu\text{m}$ is required to operate in regime I (13.56 MHz). Fabricating such a thin and leakage-free stretchable capacitor over an area on the scale of cm^2 with uniform

and precise thickness is practically difficult¹⁵. Although regime II could accommodate a less stringent requirement on Q , R_{tag} is required to be $< 300 \Omega$ under 0–50% external strain. Finally, the initial value of R_{sensor} should be on the scale of hundreds of ohms (Supplementary Fig. 3c).

Design and fabrication of individual system components

The different components that met our required specifications were realized by solution processing of stretchable materials (Fig. 3a). For conductive material, a composite ink composed of silver flakes and elastomer was chosen due to its high conductivity, low cost and printability²¹. Our obtained printed stretchable conductor provided both excellent sheet resistance ($< 50 \text{ m}\Omega \square^{-1}$) and high stretchability (Supplementary Fig. 5a). For the stretchable substrate and capacitor dielectric material, poly(styrene-*b*-ethylene-butadiene) (SEBS) was chosen because of its high stretchability, skin-like low modulus (several MPa), low leakage current and high breakdown voltage¹⁵. In addition, its good adhesion with other SEBS and printed conductors prevented layer delamination during repeated stretching cycles. The stretchable inductor was designed to adopt a spiral shape to achieve sufficiently high inductance and low resistance (Supplementary Fig. 5b). The as-designed inductor showed an initial inductance of 451.5 nH and resistance of 2.98Ω . When subjected to 50% strain, its inductance and internal resistance increased to 595.2 nH (size increase) and 41.7Ω (degradation in stretchable conductor conductivity), respectively.

The second component was the stretchable capacitor. Our capacitor showed an initial capacitance of 9.7 pF (Supplementary Fig. 5d). After stretching, the capacitance increased linearly to 18.0 pF at

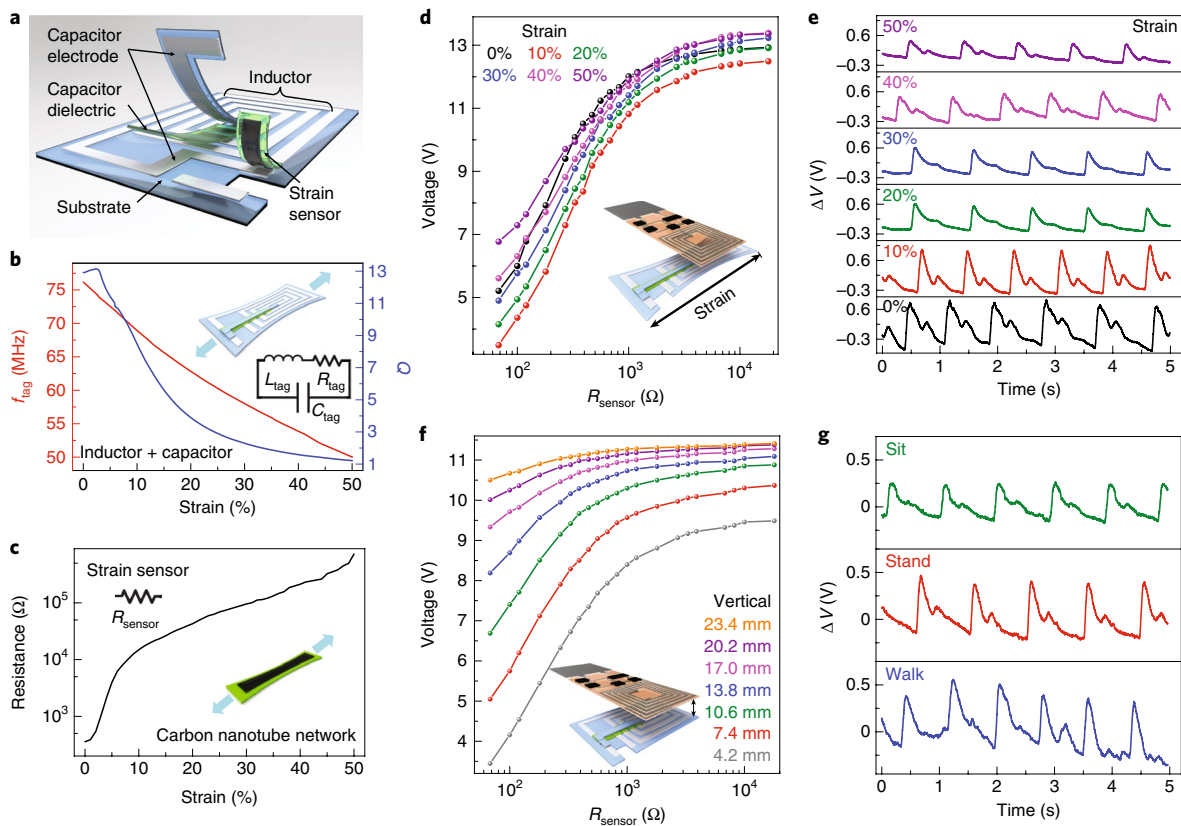


Fig. 3 | Design of the stretchable sensor target and flexible initiator. a, Schematic of the stretchable target. **b**, Stretchable antenna characteristics showing the influence of strain on f_{tag} and Q . **c**, Resistance–strain characteristics of the strain sensor. **d–g**, Robustness of the RFID system. **d**, Dependence of the output signal on sensor resistance when the target antenna is under different external strain. **e**, Human pulse signal detection (with d.c. component subtracted) by the flexible initiator when the target antenna is stretched. This was because of the technical difficulty in placing the precisely strained target on the human wrist. **f**, Dependence of the output signal on sensor resistance when the target and initiator are at different vertical separation distance. **g**, Human pulse signal detection (with d.c. component subtracted) by the flexible initiator under different application scenarios.

50% strain due to the enlarged electrode and thinned dielectric, while the series resistance was maintained at a low level ($<3\ \Omega$, Supplementary Fig. 5e). From the stretchable inductor and capacitor performance, the antenna's f_{tag} and Q could be calculated (Fig. 3b). When the strain was increased from 0 to 50%, the f_{tag} dropped from 76.2 MHz to 50.0 MHz and Q decreased from 12.9 to 1.2. Although both f_{tag} and Q changed dramatically, the system can still achieve high gain when operated in regime II.

The third component was the resistive strain sensor. A thickness-gradient carbon nanotube network was chosen as the strain-sensitive material⁹. The sensor substrate and carbon nanotube conductive material were optimized in terms of both width and concentration for better sensitivity and lower initial resistance (see Methods). After optimization of the process parameters, our obtained carbon nanotube conductive network was observed to show excellent strain sensitivity (gauge factor of 201.6 at 5% strain, high enough to detect the human pulse), high stretchability (up to 50%) and low initial resistance (357.3 Ω) (Fig. 3c).

The final component was the flexible initiator circuit (Supplementary Fig. 2a). All the necessary components for an RFID initiator were integrated into one FPCB (see Methods for detailed design). Our FPCB contains flexible batteries, antenna, oscillator, envelop detector (to generate the amplitude demodulated signal V_{out} from $V_{\text{initiator}}$), bandpass amplifier, analog-to-digital converter and microcontroller with Bluetooth transceiver. Our initiator showed excellent flexibility (could sustain a bending radius of 4 cm,

Supplementary Fig. 5i) due to the thin substrate (130 μm). Notably, the FPCB size can be further reduced by integrating the circuits into one small chip. Moreover, the integrated chip can significantly reduce power consumption, thus also decreasing the battery size.

Functionality of individual wireless sensor node

Through assembly of each developed component, our fabricated bodyNET system could effectively sense human physiological signals even when the targets were stretched to $>50\%$. Remarkably, the $V_{\text{out}}-R_{\text{sensor}}$ characteristics under different external strains were similar in behaviour, that is, maintaining a high gain even at 50% strain (Fig. 3d). Our observed results show higher values of stretchability compared with reported stretchable RFID targets^{32,33,35,37}, for which the stretchability was limited by the use of regime I and strain concentration at the chip–wire interface. As a demonstration, the weak human pulse strain signal could be detected even after 50% strain (Fig. 3e). Although the signal morphology became distorted as a result of the system nonlinearity and the small variation in initial strains applied to the on-skin sensors, it did not affect the system functionality in counting pulses thanks to the signal conditioning circuits. In addition, the stretchable RFID target showed a high durability against cyclic uniaxial strain (30%, 500 times; Supplementary Fig. 15), folding, twisting and pinching (Supplementary Fig. 14). This high mechanical and electrical durability of the stretchable target is due to the modulus matching ($\sim 1\text{--}5\ \text{MPa}$) of the utilized materials and the robust detuned system design from regime II.

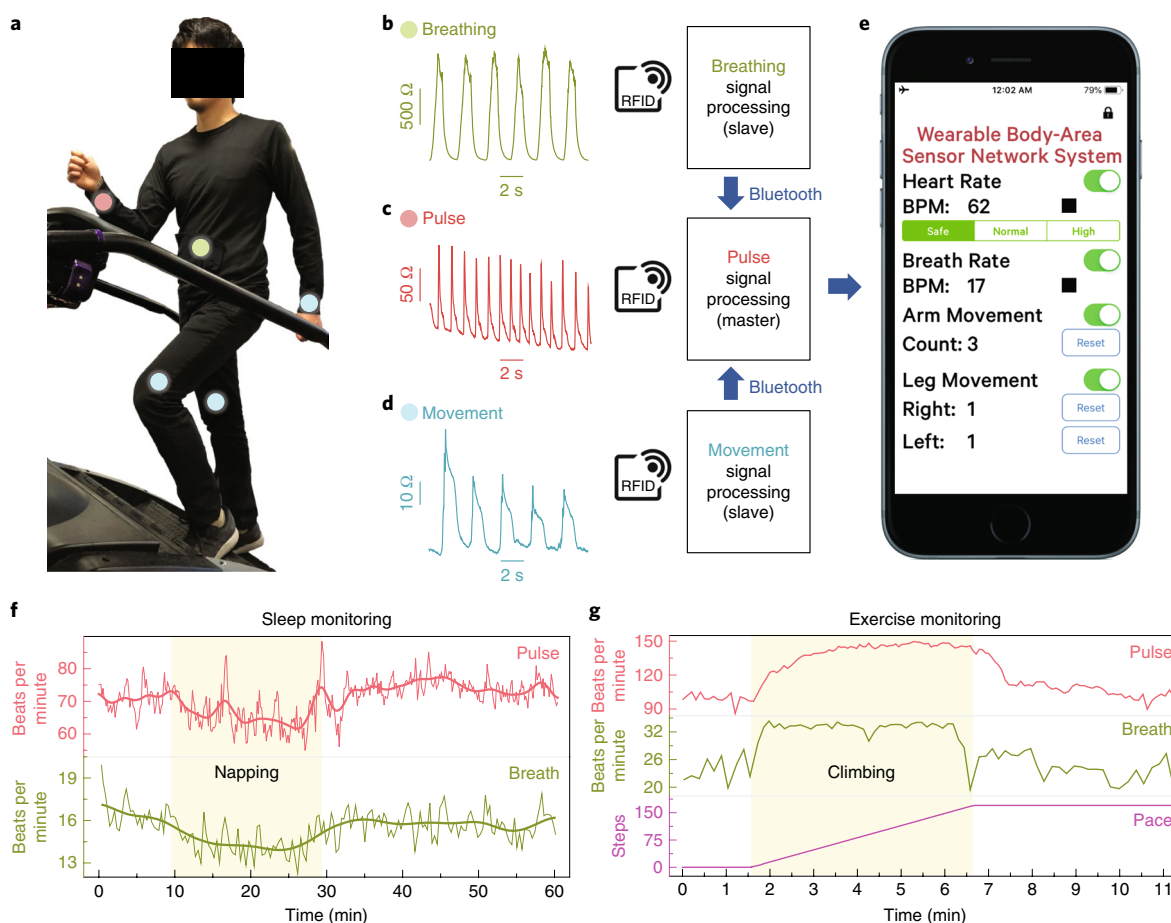


Fig. 4 | A bodyNET to measure and display human body movement, pulse and breathing simultaneously. **a**, Photograph of the bodyNET. **b–d**, Outputs from the resistive strain sensors measuring breathing (**b**), pulse (**c**) and arm movement (**d**), respectively. The data are sent to the corresponding initiators via RFID. The sensor node for the pulse collects information from the other nodes and sends it to a smartphone using Bluetooth. **e**, The smartphone user interface, which can simultaneously read out the outputs and control the bodyNET. **f**, Experimental recorded pulse and breathing rate of a subject wearing the bodyNET to perform sleep monitoring. **g**, Experimental recorded pulse rate, breathing rate and leg movement results of a subject wearing the bodyNET to perform exercise monitoring on a stair machine.

Besides its excellent strain tolerance, our bodyNET has a favourable ~ 20 – 25 mm vertical and lateral working range, thus satisfying typical usage scenarios. When the vertical separation distance increased to >20 mm, the $V_{\text{out}}-R_{\text{sensor}}$ curve became almost flat and the gain dropped to ~ 0 (Fig. 3f). This system failure resulted from the decrease in κ . The same trend was shown for the detected pulse signals (Supplementary Fig. 6a). For the lateral working range, our system could tolerate ~ 25 mm lateral antenna centre mismatch (Supplementary Fig. 6b,c). This medium working distance was preferred because it ensured that the system could maintain operation with a slight mismatch between target and initiator (for example, sliding of the clothing textile) and it also prevented signal interference between different nodes. The pulse signal can be detected under different application scenarios. Regardless of whether people are sitting, standing or walking, the pulse signal can be accurately measured by the bodyNET (Fig. 3g). The accuracy of the measured pulse signals was verified by simultaneous measurements with a commercial electrocardiogram (ECG) monitoring system (Supplementary Fig. 10). The pulse signal can also be detected from other tags with different designs (Supplementary Fig. 8) or even with some misalignment of the sensors from the artery (± 8 mm, Supplementary Fig. 11). As well as the pulse at the wrists, body movement, apex cardiograms and respiration can also be successfully detected (Supplementary Figs. 12 and 13), showing the design flexibility of our system.

Demonstration of the whole bodyNET

The bodyNET concept was realized with multiple sets of stretchable on-skin sensors and flexible readout circuits located on clothes (Fig. 4a). Our network currently contains one smartphone and five sensor nodes communicating via Bluetooth, and the number of sensors can be readily increased depending on the required application. As a demonstration of concept, one node was chosen to be located at the wrist for pulse detection (pulse node), another node at the abdomen for breath detection (breath node) and the third, fourth and fifth nodes at the elbow, left leg and right leg for body movement detection (movement nodes I, II and III). The pulse node served as master node and the other four nodes served as slave nodes. The data in the slave nodes were first gathered to the master node and the master node subsequently sent all collected data to the smartphone. The data could then be transmitted into the cloud server through the cellular network. The total signal flow is shown in Fig. 4b–e. The pulse, respiration and body movement signals were all captured by resistive strain sensors (Fig. 4b–d). The resistance changes were then wirelessly transformed through RFID and then demodulated on the flexible initiator side (Supplementary Video 1); the demodulated signals were conditioned and sent to the microcontroller for calculation of the beating and wireless transmission to smartphones. Through the smartphone user interface, all the collected pulse, respiration and body movement data can be simultaneously displayed

(Fig. 4e and Supplementary Video 2). Simultaneous measurements of pulse rate, respiration and body movement have been shown to be important in many applications, such as sleep analysis and sports physiology^{38–40}. Besides smartphones, all the captured information can also be shown in an initiator's built-in seven-segment display (Supplementary Fig. 7 and Supplementary Video 3).

Such a bodyNET is a good candidate for performing long-term, continuous, hands-free and accurate monitoring of daily physiological signals. In a first example, sleep monitoring was performed for a 1 h nap and both the pulse and respiration rate were observed to decrease during napping time (Fig. 4f and Supplementary Fig. 9a). The fluctuation in pulse and respiration rate is natural sleep behaviour and matches previous reports⁴¹. We also investigated the physiological response of subjects during physical exercise. After an initial 1.5 min stage, the subject started a 5 min stair machine exercise and then rested. The steps, pulse and respiration were simultaneously and continuously monitored using the bodyNET (Fig. 4g and Supplementary Fig. 9b). As the measured number of steps increased linearly during exercise, both pulse and respiration rate increased dramatically, then dropped quickly during the first minute of relaxation and then gradually recovered to their normal values. These two examples show the capability of our bodyNET to perform multiple-dimension, long-term, continuous and hands-free monitoring of important human physiological signals. Compared to traditional designs using Bluetooth or NFCs, our design has the advantage of having no on-skin rigid components, which improves robustness and wear comfort. Additionally, the application of our bodyNET is not restricted to specific times or locations, because it does not require user action, such as tapping smartphones to each tag or approaching body-sized antennas, for operation.

Conclusions

We have reported the design and fabrication of a bodyNET system based on battery-free and chip-free stretchable on-skin wireless sensors that are operated by flexible and wearable readout circuits. Our approach addresses the mechanical incompatibility issues between stretchable on-skin sensor devices and high-performance silicon electronics by replacing traditional physical interconnections with wireless hybridization. Deliberate detuning of RFID targets is also introduced to safeguard and protect the system from failure caused by strain-induced tag resonant frequency and quality factor variation. Our bodyNET can maintain full functionality even when subjected to 50% strain. Furthermore, the platform can continuously analyse critical human signals (pulse, respiration and body movement) and could thus potentially be used for real-time physiological and clinical investigations in a next-generation personal health monitoring system.

Methods

Materials. The hydrogenated styrenic thermoplastic elastomers (SEBS) Tuftec H1062, H1052 and H1221 were obtained from Asahi Kasei Company. The H1062 SEBS was used for the antenna and capacitor substrate, and the H1221 SEBS was used for the capacitor dielectric as well as the strain sensor substrate. The SEBS rubbers have been reported to have good long-term stability and biocompatibility¹⁵. The carbon nanotubes used for resistive strain sensors were purchased from Carbon Solutions (P3-SWNTs). The stretchable silver conductor ink was purchased from Dupont (Intexar PE873/PE874). Moisture-resistant 100- μm -thick polyethylene terephthalate (PET) was purchased from McMaster–Carr.

Fabrication of stretchable inductors, capacitors and strain sensors. The fabrication of a stretchable target is shown in Supplementary Fig. 1. The SEBS (H1062 and H1221) was first dissolved in toluene to form a solution (150 mg ml⁻¹), then the solution was dropcast on a glass slide to form a SEBS film. The stretchable inductor pattern and the stretchable capacitor bottom electrode were fabricated by stencil printing of Dupont stretchable silver conductor ink (Intexar PE873/PE874) on the H1062 SEBS substrate (layer 1, Supplementary Fig. 1c). After removal of the stencil, the ink was cured at 110 °C for 10 min. The top electrode of the stretchable capacitor was fabricated with the same method on another H1062 SEBS substrate (layer 2). A ~100 μm H1221 SEBS was then laminated on the first substrate to serve

as the capacitor dielectric (Supplementary Fig. 1d). Next, we laminated layer 2 on top of the H1221 capacitor dielectric. Finally, at the interface between the two layers, additional Dupont ink was applied and the ink was cured again at 110 °C for 10 min to form stable electrical connection between layers 1 and 2 (Supplementary Fig. 1e).

P3-SWNT carbon nanotubes were dispersed with deionized water to form carbon nanotube solutions with different concentrations (0.2 mg ml⁻¹ to 2 mg ml⁻¹). The solution was sonicated for 2 h to uniformly disperse the carbon nanotubes. The strain sensor substrate was made of ~100 μm H1221 SEBS. A 100 μm PET mask was patterned using a Silhouette Cameo cutter and applied on the H1221 substrate, then the substrate was treated with oxygen plasma (Technics Miro-RIE Series 800, 150 W, 15 s) to make the uncovered SEBS area hydrophilic. The carbon nanotube water solution was dropped onto the hydrophilic SEBS area and the whole substrate was dried at room temperature until the water had thoroughly evaporated. Finally, the fabricated strain sensor was directly laminated to the specifically designed port in the antenna area (Supplementary Fig. 1f).

The overall dimensions of the stretchable inductor inside the target were 51.6 mm \times 43.2 mm. The inductor had a spiral shape. The conductor width could vary between 3 mm and 4 mm and the gap between conductor lines could vary between 1 mm and 2 mm. The capacitor electrode size was 12.2 mm \times 5.6 mm. As well as the typical tag design, we also fabricated other tags with different shapes. Their overall dimensions were 26 mm \times 25 mm (octagonal shape), 30 mm \times 31 mm (square shape) and 70 mm \times 25 mm (wrist band shape), respectively. For the octagonal tags, both the conductor width and the gap between each conductor line were 0.51 mm. For the other two designs, the conductor width was 1.5 mm and the gap between each conductor line was 0.76 mm.

Design of the flexible RFID initiator circuit. The flexible RFID initiator silicon circuit comprised two batteries, a power management circuit to provide a constant voltage bias, a 13.56 MHz oscillator, an initiator antenna with matching circuit, an envelope detector for demodulation of the received signal, a bandpass amplifier, a 1 bit analog-to-digital converter (ADC) and a microcontroller for central signal computation and transmission. The design of each component is described in the following sections.

Initiator antenna design. The initiator antenna was designed with a five-turn spiral shape, and its dimensions were 44 mm \times 46 mm. Each conductor line width was 1.27 mm and the gap between every two conductor lines was also 1.27 mm. The antenna had an inductance of 1.2 μH . An external resistance was added to increase the internal inductor resistance to ~2.45 Ω , which reduced the antenna quality factor to an optimum value of ~40.

Oscillators and initiator antenna matching circuit. A 13.56 MHz oscillator was utilized to drive the initiator antenna. The oscillator diagram is shown in Supplementary Fig. 2c. The oscillator was based on a comparator (Linear Technology LT1016) with a crystal as positive feedback. The crystal was used to provide a stable oscillation frequency. The oscillators were able to generate a 3 V square-wave output with 9.1 Ω output resistance. A low-pass electromagnetic compatibility (EMC) filter (L_1 and $C_{\text{match}1}$) was added to filter out the unnecessary high-order harmonics in the square-wave oscillator output, and a capacitor bridge network ($C_{\text{match}2}$ and $C_{\text{match}3}$) was added for impedance matching to deliver the maximum available power to the initiator antenna³⁶.

Signal processing and conditioning circuit. The RFID load modulation mechanism was utilized for wireless transmission of the strain sensor signal from the stretchable target side. As a result, the received signal on the flexible initiator side was an amplitude-modulated signal, which could be demodulated by an envelope detector (D_1 , C_7 and R_{15} in Supplementary Fig. 2d). After envelope detection, the carrier signal was removed and the remaining signal passed through a bandpass amplifier for conditioning (Supplementary Fig. 2d). The bandpass amplifier included two stages: a high-pass Butterworth amplifier with a -3 dB corner frequency of ~0.05 Hz and a low-pass Butterworth amplifier with a -3 dB corner frequency of 40 Hz. The high-pass filter was utilized to remove the d.c. component of the signal while the low-pass filter was utilized to filter out the remaining carrier signal and noise. The amplifier in each stage was designed with Sallen–Key topology to provide filtering and amplification at the same stage⁴².

After amplification, the signal passed through an ADC. The 1 bit ADC was designed with one comparator, as shown in Supplementary Fig. 2d. To avoid the signal fluctuation generated from input signal noise, hysteresis was added through positive feedback and an inverter was further used to buffer the signal and remove the fluctuation.

Microcontrollers and Bluetooth communication system. We designed two versions of the RFID initiator circuits, one with Bluetooth functionality and one with a built-in seven-segment display. For the version with Bluetooth, the core of the system was a Simelec microcontroller (RFD77101, RF Digital Corporation) with built-in Bluetooth transceiver and integrated Bluetooth antenna. For the version with a built-in seven-segment display, the microcontroller was an Atmel Atmega32u4 microcontroller. Both microcontrollers are compatible with the Arduino programming environment.

The bodyNET smartphone user interface was designed with the Siblee-for-mobile application platform. To use this smartphone interface, the user opened the smartphone Siblee application, which is compatible with both IOS and Android mobile systems. A secure Bluetooth connection was thus established between the smartphone and the Siblee microcontroller inside the master sensor node. Bluetooth connection was also established between the Siblee microcontroller inside the master sensor node and the Siblee microcontroller inside each slave node. Once the data stored in the sensor nodes were updatable, the stream of data from the slave sensing node was first transmitted to the master node, then the master node gathered the data and transmitted the dataset to the smartphone. The breathing rate, pulse rate and body movement count could be displayed on the cellphone screen. In addition, the function on/off switches and the reset button for body movement counting were also included in the application for user control of the bodyNET.

Power supply and regulation for the flexible RFID initiator circuit. The flexible RFID initiator circuit was powered by two ultrathin flexible lithium-polymer batteries in series (Power Streams, PGEB014461, $1 \times 44 \times 61$ mm³, 3.7 V, 200 mAh capacity). Separate linear voltage regulators were used to generate the individual 5 V, 3.3 V and 2.5 V output voltages (Supplementary Fig. 2b). The 5 V output served as voltage source for the oscillators, bandpass filters, ADCs and Atmel Atmega32u4 microcontrollers. The 3.3 V output provided the voltage supply for the Siblee microcontrollers. Finally, the 2.5 V voltage output served as a voltage reference to be used in the bandpass amplifiers. A detailed power regulation diagram is shown in Supplementary Fig. 2e.

Circuit simulation. The RFID circuit diagram used in the simulation is shown in Supplementary Fig. 3a. The right initiator side included the 13.56 MHz oscillator, the EMC filter ($L_{\text{match}1}$ and $C_{\text{match}1}$), the impedance matching circuit ($C_{\text{match}2}$ and $C_{\text{match}3}$) and the initiator antenna ($L_{\text{initiator}}$ and $R_{\text{initiator}}$). The oscillator and initiator antenna parameters were experimentally measured while the EMC filter and impedance matching circuit were designed accordingly to maximize the transferred power from the oscillator to the initiator antenna³⁶. The target antenna simulation parameters were determined from the experimental measurement results of the printed target antenna at 0% strain. The final simulation parameters are shown in Supplementary Table 1. In the simulation, we made an assumption that the output impedance of the oscillator was purely resistive to simplify the equivalent circuit model for the oscillator. This assumption will not affect the obtained conclusion, but the impedance matching network in the experiment will have different values from the simulation.

The circuit simulation was entirely performed using HSPICE simulation software with the transient analysis module. The total simulation period was 6.5 μ s and the simulation time interval was 0.1 ns. The data were collected after a steady state was reached (from 6 μ s to 6.5 μ s). The simulation results for the signal received on the initiator antenna are shown in Supplementary Fig. 3b. The amplitude of the a.c. signal was extracted ($|V_{\text{initiator}}|$) and is displayed in Fig. 2b. The slope of the $|V_{\text{initiator}}| - R_{\text{sensor}}$ curve increases with decreasing R_{sensor} , as confirmed in the calculated gain data shown in Supplementary Fig. 3c. The gain at $R_{\text{sensor}} = 700 \Omega$ is used in the following discussions. Supplementary Fig. 3d shows the simulation results when $\kappa = 0.5$. In this case, the gain in regime I is already small and the peak gain in regime I has shifted to the lower frequency side, so the gain at $f_{\text{tag}} = 12$ MHz is higher than the gain at 13.56 MHz. More data describing the influence of κ , Q , f_{tag} and L_{tag} on the gain are shown in Supplementary Fig. 3d–i. From these data, it is clearly observed that the detuned target has a better tolerance for Q and f_{tag} change.

Experimental verification of the system design. The experimental verification was performed using an FPCB initiator with a rigid PCB antenna that has the same antenna pattern as the stretchable target. The experimental set-up is shown in Supplementary Fig. 4a. In the rigid PCB antenna, accurate surface-mounted ceramic capacitors were used to control f_{tag} and surface-mounted resistors were used to control the target quality factor (Supplementary Fig. 4b). The d.c. voltage on the FPCB initiator side after envelope detection was measured with different resistors and capacitors applied. The measurement results in Fig. 2e were measured with the target and initiator separated with a vertical separation distance of 12 mm. These medium coupling conditions show both regime I and regime II. The measurement results under tight coupling conditions (3 mm vertical separation distance) are shown in Supplementary Fig. 4c. In this case, the gain in regime I is already very low due to the strong target loading effect. In addition, the peak for the gain in regime I shifts to the lower frequency side and will not be exactly 13.56 MHz, consistent with the simulation results. To measure the Q tolerance for each regime, the $V_{\text{out}} - R_{\text{sensor}}$ curves of two representative cases were measured and are shown in Supplementary Fig. 4d,e when changing Q from 26.22 to 0.06. For regime I, f_{tag} was set to 13.6 MHz and the separation distance was 21 mm. For regime II, f_{tag} was set to 64.9 MHz and the separation distance was 6 mm. From these curves, we can calculate the slope at 700 Ω and plot the gain data as shown in Fig. 2f.

The experimental results show exactly the same trend as the theoretical simulation results, with slight numerical differences. First, the coupling factor in the experimental results was not exactly the same as the values used in the

simulations. Second, the simulation results in Fig. 2b,d show the amplitude of the a.c. signal received at the readout antenna. In contrast, the voltage results in Fig. 2e,f show the d.c. voltage after envelope detection circuits, not the a.c. voltage amplitude of the received signal. These two signals will have a difference in the diode conduction voltage. Third, the output impedance of the oscillator used in the experiment was not purely resistive, but in the simulation we made this assumption to simplify the equivalent circuit model for the oscillator. This difference will not affect the conclusion, but the impedance matching network in the experiment will have different values from the simulated values.

Device characterization. The stretchable inductor, capacitor and strain sensor characterizations were performed with a precision LCR meter (Keysight E4980A). The inductor and capacitor were characterized with the equipment's maximal operation frequency (2 MHz) while the resistive strain sensor was characterized under the equipment's lowest operation frequency (20 Hz). The d.c. voltage value of the demodulated signal was measured by a Fluke 8808A multimeter. The original pulse, breathing and arm movement signals from the resistive strain sensor were captured by a Semiconductor Characterization System (Keithley 4200). After wireless transmission via RFID and demodulation with the flexible initiator, the real-time demodulated heart rate signal shown in Fig. 3e,g and Supplementary Fig. 6a,c was collected by a mixed-signal oscilloscope (Keysight MSOX4154A) with a 20 Hz low-pass filter.

Optimization of the strain sensor. The strain sensor substrate and the carbon nanotube pattern (width and solution concentration) were two important factors in determining the strain sensor performance. First, the influence of the SEBS substrate was examined. As a first step, we compared three different commonly utilized SEBS substrates with different chemical compositions. As shown in Supplementary Fig. 5f, the SEBS with lower modulus was found to offer better sensitivity. This is because the stress is easier to concentrate at initial carbon nanotube cracks when the substrate modulus is smaller. Finally, a ~ 100 μ m H1221 SEBS was chosen as the substrate as a compromise between sensor sensitivity and handling ability. Besides the sensor substrate, the carbon nanotube solution concentration and sensor width also had a significant effect on sensor performance. The choice of carbon nanotube concentration was determined as a compromise between the sensor initial resistance (Supplementary Fig. 5h) and dispersion ability. The selection of sensor width was based on both the initial resistance and sensitivity (Supplementary Fig. 5g). Finally, a width of 2 mm and 2 mg ml⁻¹ carbon nanotube solution were selected to achieve better sensor performance. With this optimization, the strain sensor was able to achieve both high sensitivity and low initial resistance and thus satisfy the requirements for system integration.

Testing the devices on human bodies. The Institutional Review Board office at Stanford University determined that this project (protocol no. IRB-48874) does not meet the definition of human subject research as defined in federal regulations 45 CFR 46.102 or 21 CFR 50.3. The skin shown in the figures and videos are those of S. Niu and N. Matsuhisa, who have given their consent to publish these images and videos.

To test the bodyNET system on human bodies, we first attached a layer of 3M Tegaderm film (an FDA-approved medical-grade biocompatible adhesive dressing) on the desired skin area and then attached the sensor tag on top of the film. Finally, another layer of 3M Tegaderm film that covered the sensor tag was attached to fix the tag position. This arrangement was able to tolerate mild perspiration and body temperature changes. The FPCB was attached on the outer side of the subjects' clothes with double-sided tape. The initiator could be attached in this way as long as the textiles were not extremely rough. However, the initiator could also be placed inside a hidden thin pocket on the clothing, so there is actually no limitation on textile choice. These attachment methods allowed us to easily remove the initiator from the textiles for washing. Data transmission is not affected by the textiles as long as they are not highly conductive. For parts of the body that are not normally covered by clothes, such as the wrist, the FPCB could be located in a wristband or as watch-like electronics. The FPCB antenna centre should coincide with the sensor tag antenna to maximize the coupling factor. Finally, we covered the FPCB with another layer of black cloth to make the FPCB 'invisible'. The 3M Tegaderm film prevented direct contact of the stretchable sensors with the skin, so the effect of sweat could be reduced. We could also add some commercially available water and sweat-proof adhesive to improve the adhesion if the sensing system were to be used in very sweaty conditions.

Validation of the physiological measurement. The respiration and body movement measurements can be easily validated, as shown in Supplementary Videos 2, 3 and 4. In these videos, synchronization of light from a light-emitting diode with the external mechanical motion provides clear evidence of correct measurements. The validity of our heart rate measurements was confirmed by simultaneously monitoring the heart rate using both a commercial ECG monitoring system (SparkFun Single Lead Heart Rate Monitor based on an Analog Devices AD8232 amplifier) and our sensing system. Two commercial hydrogel electrodes (3M Red Dot electrocardiogram electrodes), located on the left and right

arms, were utilized to collect the ECG signal. The amplified signal was measured using an oscilloscope. As shown in Supplementary Fig. 10, our sensor showed exactly the same number of peaks as the commercial sensor. We also analysed the frequency spectrum of the two signals. For both signals, the frequency spectrum peak is located at 1.06 Hz. The heart rate can be calculated as 63.6 beats per minute, showing that the results obtained using our system are correct.

Reporting Summary. Further information on research design is available in the Nature Research Reporting Summary linked to this article.

Data availability

The data that support the plots within this paper and other findings of this study are available from the corresponding authors upon reasonable request.

Received: 16 December 2018; Accepted: 17 July 2019;

Published online: 15 August 2019

References

- Yang, G. Z. *Body Sensor Networks* 2nd edn (Springer, 2014).
- Hanson, M. A. et al. Body area sensor networks: challenges and opportunities. *Computer* **42**, 58–65 (2009).
- Chu, B., Burnett, W., Chung, J. W. & Bao, Z. Bring on the bodyNET. *Nature* **549**, 328–330 (2017).
- Gao, W. et al. Fully integrated wearable sensor arrays for multiplexed in situ perspiration analysis. *Nature* **529**, 509–514 (2016).
- Mukhopadhyay, S. C. Wearable sensors for human activity monitoring: a review. *IEEE Sens. J.* **15**, 1321–1330 (2015).
- Lee, H. et al. A graphene-based electrochemical device with thermoresponsive microneedles for diabetes monitoring and therapy. *Nat. Nanotechnol.* **11**, 566–572 (2016).
- Son, D. et al. Multifunctional wearable devices for diagnosis and therapy of movement disorders. *Nat. Nanotechnol.* **9**, 397–404 (2014).
- Yang, S. X. et al. 'Cut-and-paste' manufacture of multiparametric epidermal sensor systems. *Adv. Mater.* **27**, 6423–6430 (2015).
- Liu, Z. Y. et al. Thickness-gradient films for high gauge factor stretchable strain sensors. *Adv. Mater.* **27**, 6230–6237 (2015).
- Kim, J., Kumar, R., Bando, A. J. & Wang, J. Advanced materials for printed wearable electrochemical devices: a review. *Adv. Electron. Mater.* **3**, 1600260 (2017).
- Liu, W., Song, M. S., Kong, B. & Cui, Y. Flexible and stretchable energy storage: recent advances and future perspectives. *Adv. Mater.* **29**, 1603436 (2017).
- Zamarayeva, A. M. et al. Flexible and stretchable power sources for wearable electronics. *Sci. Adv.* **3**, e1602051 (2017).
- Yi, F. et al. A highly shape-adaptive, stretchable design based on conductive liquid for energy harvesting and self-powered biomechanical monitoring. *Sci. Adv.* **2**, e1501624 (2016).
- Kaltenbrunner, M. et al. Ultrathin and lightweight organic solar cells with high flexibility. *Nat. Commun.* **3**, 770 (2012).
- Wang, S. H. et al. Skin electronics from scalable fabrication of an intrinsically stretchable transistor array. *Nature* **555**, 83–88 (2018).
- Andrews, J. B. et al. Patterned liquid metal contacts for printed carbon nanotube transistors. *ACS Nano* **12**, 5482–5488 (2018).
- Park, M. et al. Highly stretchable electric circuits from a composite material of silver nanoparticles and elastomeric fibres. *Nat. Nanotechnol.* **7**, 803–809 (2012).
- Larson, C. et al. Highly stretchable electroluminescent skin for optical signaling and tactile sensing. *Science* **351**, 1071–1074 (2016).
- Liang, J. J., Li, L., Niu, X. F., Yu, Z. B. & Pei, Q. B. Elastomeric polymer light-emitting devices and displays. *Nat. Photon.* **7**, 817–824 (2013).
- Keplinger, C. et al. Stretchable, transparent, ionic conductors. *Science* **341**, 984–987 (2013).
- Matsuhisa, N. et al. Printable elastic conductors by in situ formation of silver nanoparticles from silver flakes. *Nat. Mater.* **16**, 834–840 (2017).
- Trung, T. Q. & Lee, N. E. Flexible and stretchable physical sensor integrated platforms for wearable human-activity monitoring and personal healthcare. *Adv. Mater.* **28**, 4338–4372 (2016).
- Hartmann, F., Drack, M. & Kaltenbrunner, M. Meant to merge: fabrication of stretchy electronics for robotics. *Sci. Robot.* **3**, eaat9091 (2018).
- Sekitani, T. et al. Stretchable active-matrix organic light-emitting diode display using printable elastic conductors. *Nat. Mater.* **8**, 494–499 (2009).
- Kim, D. H. et al. Epidermal electronics. *Science* **333**, 838–843 (2011).
- Valentine, A. D. et al. Hybrid 3D printing of soft electronics. *Adv. Mater.* **29**, 1703817 (2017).
- van den Brand, J. et al. Flexible and stretchable electronics for wearable health devices. *Solid State Electron.* **113**, 116–120 (2015).
- Xu, S. et al. Soft microfluidic assemblies of sensors, circuits, and radios for the skin. *Science* **344**, 70–74 (2014).
- Huang, Z. et al. Three-dimensional integrated stretchable electronics. *Nat. Electron.* **1**, 473–480 (2018).
- Graz, I. M., Cotton, D. P. J., Robinson, A. & Lacour, S. P. Silicone substrate with in situ strain relief for stretchable thin-film transistors. *Appl. Phys. Lett.* **98**, 124101 (2011).
- Vanfleteren, J. et al. Printed circuit board technology inspired stretchable circuits. *MRS Bull.* **37**, 254–260 (2012).
- Han, S. et al. Battery-free, wireless sensors for full-body pressure and temperature mapping. *Sci. Transl. Med.* **10**, eaan4950 (2018).
- Kim, J. et al. Battery-free, stretchable optoelectronic systems for wireless optical characterization of the skin. *Sci. Adv.* **2**, e1600418 (2016).
- Bandodkar, A. J. et al. Battery-free, skin-interfaced microfluidic/electronic systems for simultaneous electrochemical, colorimetric, and volumetric analysis of sweat. *Sci. Adv.* **5**, eaav3294 (2019).
- Kim, J. et al. Epidermal electronics with advanced capabilities in near-field communication. *Small* **11**, 906–912 (2015).
- Paret, D. *Antenna Designs for NFC Devices* (Wiley, 2016).
- Huang, X. et al. Stretchable, wireless sensors and functional substrates for epidermal characterization of sweat. *Small* **10**, 3083–3090 (2014).
- Brink, M., Muller, C. H. & Schierz, C. Contact-free measurement of heart rate, respiration rate, and body movements during sleep. *Behav. Res. Methods* **38**, 511–521 (2006).
- Chen, W. X. et al. Unconstrained monitoring of long-term heart and breath rates during sleep. *Physiol. Meas.* **29**, N1–N10 (2008).
- Dong, J. G. The role of heart rate variability in sports physiology. *Exp. Ther. Med.* **11**, 1531–1536 (2016).
- Bunde, A. et al. Correlated and uncorrelated regions in heart-rate fluctuations during sleep. *Phys. Rev. Lett.* **85**, 3736–3739 (2000).
- Sallen, R. P. & Key, E. L. A practical method of designing RC active filters. *IEEE Trans. Circuit Theory* **2**, 74–85 (1955).

Acknowledgements

This research was supported by Samsung Electronics. X.C. acknowledges financial support from the Agency for Science, Technology and Research (A*STAR) under its AME Programmatic Funding Scheme (project no. A18A1b0045). N.M. acknowledges funding support from an overseas fellowship from the Japan Society for the Promotion of Science (JSPS). A.S.Y.P., Z.B. and N.M. acknowledge support from Stanford Precision Health and Integrated Diagnosis Center for seed funding support. The authors thank S. Taheri, W. Wang, J. Kim, B. Chu, Y. Zheng, J. Kang, Y. Kim, H.-C. Wu, J. Xu, T. Lei, Y. Liu, Z. Liu, G. Chen, Y. Jiang and B. Murrmann for experimental assistance and insightful discussions. The authors also thank Dupont for providing the stretchable conductor inks.

Author contributions

S.N., N.M., W.B. and Z.B. generated the design concept. S.N. designed the overall system architecture and verified this architecture through circuit simulation. S.N. designed, fabricated and tested the flexible readout circuits. S.N. and N.M. fabricated the intrinsically stretchable sensor tags, developed the Bluetooth user interfaces and performed all the system measurements and daily physiological signal monitoring. L.B. helped in the design and fabrication of strain sensors. N.M., S.N., Y.Y. and J.L. helped to prepare the three-dimensional schematics and carried out device photography. S.W., J.W., Y.J. and X.Y. contributed to the material choice of stretchable tags. A.S.Y.P. commented on the RFID system design. S.N., N.M., Z.B. and J.B.-H.T. wrote the manuscript. Z.B. and X.C. supervised the project. All authors reviewed and commented on the manuscript.

Competing interests

A patent based on this research has been submitted.

Additional information

Supplementary information is available for this paper at <https://doi.org/10.1038/s41928-019-0286-2>.

Reprints and permissions information is available at www.nature.com/reprints.

Correspondence and requests for materials should be addressed to X.C. or Z.B.

Publisher's note: Springer Nature remains neutral with regard to jurisdictional claims in published maps and institutional affiliations.

© The Author(s), under exclusive licence to Springer Nature Limited 2019

Reporting Summary

Nature Research wishes to improve the reproducibility of the work that we publish. This form provides structure for consistency and transparency in reporting. For further information on Nature Research policies, see [Authors & Referees](#) and the [Editorial Policy Checklist](#).

Statistics

For all statistical analyses, confirm that the following items are present in the figure legend, table legend, main text, or Methods section.

- | n/a | Confirmed |
|-------------------------------------|---|
| <input checked="" type="checkbox"/> | <input type="checkbox"/> The exact sample size (n) for each experimental group/condition, given as a discrete number and unit of measurement |
| <input checked="" type="checkbox"/> | <input type="checkbox"/> A statement on whether measurements were taken from distinct samples or whether the same sample was measured repeatedly |
| <input checked="" type="checkbox"/> | <input type="checkbox"/> The statistical test(s) used AND whether they are one- or two-sided
<i>Only common tests should be described solely by name; describe more complex techniques in the Methods section.</i> |
| <input checked="" type="checkbox"/> | <input type="checkbox"/> A description of all covariates tested |
| <input checked="" type="checkbox"/> | <input type="checkbox"/> A description of any assumptions or corrections, such as tests of normality and adjustment for multiple comparisons |
| <input checked="" type="checkbox"/> | <input type="checkbox"/> A full description of the statistical parameters including central tendency (e.g. means) or other basic estimates (e.g. regression coefficient) AND variation (e.g. standard deviation) or associated estimates of uncertainty (e.g. confidence intervals) |
| <input checked="" type="checkbox"/> | <input type="checkbox"/> For null hypothesis testing, the test statistic (e.g. F , t , r) with confidence intervals, effect sizes, degrees of freedom and P value noted
<i>Give P values as exact values whenever suitable.</i> |
| <input checked="" type="checkbox"/> | <input type="checkbox"/> For Bayesian analysis, information on the choice of priors and Markov chain Monte Carlo settings |
| <input checked="" type="checkbox"/> | <input type="checkbox"/> For hierarchical and complex designs, identification of the appropriate level for tests and full reporting of outcomes |
| <input checked="" type="checkbox"/> | <input type="checkbox"/> Estimates of effect sizes (e.g. Cohen's d , Pearson's r), indicating how they were calculated |

Our web collection on [statistics for biologists](#) contains articles on many of the points above.

Software and code

Policy information about [availability of computer code](#)

Data collection

No commercial nor open source code used for data collection. The only exception is the code to for the microcontroller to process and send the collected data.

Data analysis

No commercial nor open source for data analysis. The only exception is the Matlab code for basic signal analysis such as signal filtering.

For manuscripts utilizing custom algorithms or software that are central to the research but not yet described in published literature, software must be made available to editors/reviewers. We strongly encourage code deposition in a community repository (e.g. GitHub). See the Nature Research [guidelines for submitting code & software](#) for further information.

Data

Policy information about [availability of data](#)

All manuscripts must include a [data availability statement](#). This statement should provide the following information, where applicable:

- Accession codes, unique identifiers, or web links for publicly available datasets
- A list of figures that have associated raw data
- A description of any restrictions on data availability

Provide your data availability statement here.

Field-specific reporting

Please select the one below that is the best fit for your research. If you are not sure, read the appropriate sections before making your selection.

- Life sciences Behavioural & social sciences Ecological, evolutionary & environmental sciences

Life sciences study design

All studies must disclose on these points even when the disclosure is negative.

Sample size	Sample is selected within the authors. No sample size calculation is calculated due to the nature of electronics research.
Data exclusions	No data were excluded from the analyses
Replication	All experimental findings were reliably reproduced.
Randomization	The randomization is not relevant to this study due to the nature of electronics research.
Blinding	The investigators were not blinded.

Reporting for specific materials, systems and methods

We require information from authors about some types of materials, experimental systems and methods used in many studies. Here, indicate whether each material, system or method listed is relevant to your study. If you are not sure if a list item applies to your research, read the appropriate section before selecting a response.

Materials & experimental systems

n/a	Involvement in the study
<input checked="" type="checkbox"/>	<input type="checkbox"/> Antibodies
<input checked="" type="checkbox"/>	<input type="checkbox"/> Eukaryotic cell lines
<input checked="" type="checkbox"/>	<input type="checkbox"/> Palaeontology
<input checked="" type="checkbox"/>	<input type="checkbox"/> Animals and other organisms
<input type="checkbox"/>	<input checked="" type="checkbox"/> Human research participants
<input checked="" type="checkbox"/>	<input type="checkbox"/> Clinical data

Methods

n/a	Involvement in the study
<input checked="" type="checkbox"/>	<input type="checkbox"/> ChIP-seq
<input checked="" type="checkbox"/>	<input type="checkbox"/> Flow cytometry
<input checked="" type="checkbox"/>	<input type="checkbox"/> MRI-based neuroimaging

Human research participants

Policy information about [studies involving human research participants](#)

Population characteristics	Two of the authors, Dr. Simiao Niu and Dr. Naoji Matsuhisa are involved in the test of the body area sensor networks functionality.
Recruitment	The two testers are within the authors of the current manuscript.
Ethics oversight	The Institutional Review Board (IRB) office in Stanford University has determined that this project (Protocol Number: IRB-48874) does not meet the definition of human subject research as defined in federal regulations 45 CFR 46.102 or 21 CFR 50.3.

Note that full information on the approval of the study protocol must also be provided in the manuscript.